ELSEVIER

Contents lists available at ScienceDirect

Chemosphere

journal homepage: www.elsevier.com/locate/chemosphere



Secondary organic aerosol formation from atmospheric reactions of anisole



Chunlin Li^{a,**}, Maria V. Misovich^b, Michal Pardo^a, Zheng Fang^a, Alexander Laskin^b, Jianmin Chen^c, Yinon Rudich^{a,*}

- ^a Department of Earth and Planetary Sciences, Weizmann Institute of Science, Rehovot, 76100, Israel
- ^b Department of Chemistry, Purdue University, West Lafayette, IN, 47907, United States

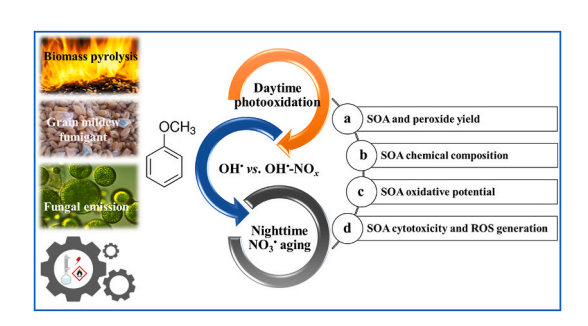
and associated health effects

^c Shanghai Key Laboratory of Atmospheric Particle Pollution and Prevention, Department of Environmental Science and Engineering, Institute of Atmospheric Sciences, Fudan University, Shanghai, 200438, China

HIGHLIGHTS

- Anisole has high and varying SOA yields against OH.•-NO_x and NO₃• reaction pathways and aging degrees.
- Anisole photooxidation produces highly-oxygenated and low-volatility compounds resulting from ring-opening reactions.
- Fresher photochemically-generated anisole SOA are more light absorbing and have higher OP, organoperoxide content, and reactivity towards NO₃.
- High NO_x levels lower the OP and organoperoxides composition of anisole SOA in photooxidation.
- Nighttime NO₃. aging modifies the properties and toxicity of photochemically-generated anisole SOA.

GRAPHICAL ABSTRACT



ARTICLE INFO

Handling editor: Volker Matthias

Keywords:
Methoxybenzene
Photochemical oxidation
NO₃● aging
SOA yield
Oxidative potential
Cytotoxicity

ABSTRACT

Anisole (methoxybenzene) represents an important marker compound of lignin pyrolysis and a starting material for many chemical products. In this study, secondary organic aerosols (SOA) formed by anisole via various atmospheric processes, including homogeneous photooxidation with varying levels of $OH \bullet$ and NO_x and subsequent heterogeneous $NO_3 \bullet$ dark reactions, were investigated. The yields of anisole SOA, particle-bound organoperoxides, particle-induced oxidative potential (OP), and cytotoxicity were characterized in view of the atmospheric fate of the anisole precursor. Anisole SOA yields ranged between 0.12 and 0.35, depending on the reaction pathways and aging degrees. Chemical analysis of the SOA suggests that cleavage of the benzene ring is the main reaction channel in the photooxidation of anisole to produce low-volatility, highly oxygenated small molecules.

Fresh anisole SOA from OH• photooxidation are more light-absorbing and have higher OP and organoperoxide content. The high correlation between SOA OP and organoperoxide content decreases exponentially with the

E-mail addresses: chunlin.li@weizmann.ac.il (C. Li), yinon.rudich@weizmann.ac.il (Y. Rudich).

^{*} Corresponding author.

^{**} Corresponding author.

degree of OH• aging. However, the contribution of organoperoxides to OP is minor (<4%), suggesting that other, non-peroxide oxidizers play a central role in anisole SOA OP. The particle-induced OP and particulate organoperoxides yield both reach a maximum value after \sim 2 days' of photooxidation, implicating the potential long impact of anisole during atmospheric transport. NO_x-involved photooxidation and nighttime NO₃• reactions facilitate organic nitrate formation and enhance particle light absorption. High NO_x levels suppress anisole SOA formation and organoperoxides yield in photooxidation, with decreased aerosol OP and cellular oxidative stress. In contrast, nighttime aging significantly increases the SOA toxicity and reactive oxygen species (ROS) generation in lung cells. These dynamic properties and the toxicity of anisole SOA advocate consideration of the complicated and consecutive aging processes in depicting the fate of VOCs and assessing the related effects in the atmosphere.

1. Introduction

Lignin pyrolysis during wood burning generates high concentrations of volatile organic compounds (VOCs) in smoke plumes. These compounds can affect atmospheric chemistry and human health regionally and globally (Chen et al., 2017; Hatch et al., 2015; Xu et al., 2020). Anisole (C₇H₈O, methoxybenzene, MB) is one of the main phenolic ethers released into the atmosphere by biomass burning, and its emission is comparable to those of polyaromatic hydrocarbons (PAHs) (Gilman et al., 2015; Hatch et al., 2015; Sekimoto and Koss, 2021; Sun et al., 2016). In light of the large amount and increasing trend of domestic biofuel use and vegetation fires (200 TgC yr⁻¹), emissions of anisole and its derivatives have become substantially significant (Akinrinola et al., 2014; Hatch et al., 2015; Li et al., 2017). In addition to biomass burning emissions, anisole is also emitted by microorganisms, insects, and the pharmaceutical and other industries, such as MB-based essences and detergents for indoor environments and fumigants for postharvest pest control in fields and silos (Betancourt et al., 2013; Fischer et al., 2000; Schuchardt and Kruse, 2009; Toloza et al., 2006; Yang and Liu, 2021). Anisole is an important starting material for many volatile chemical products (VCPs) and intermediate compounds in organic synthesis, cosmetics, and pharmaceuticals (Arivazhagan et al., 2013; Fiege et al., 2000; Seitz and Ram, 2000; SriBala et al., 2019). Additionally, anisole has been considered a surrogate for lignocellulosic pyrolysis biofuel and a promising bio-blend stock because of its flammability, high energy density, eco-friendliness, and sustainability (Wagnon et al., 2018, 2017; Wojcieszyk et al., 2021; Wu et al., 2017). All these factors indicate the growing importance of anisole pollution. However, anisole has largely been overlooked in atmospheric and air quality research.

The main atmospheric sinks of phenolic VOCs are reactions with oxidants, including ozonolysis, daytime photooxidation by OH•, usually influenced by NO_x in polluted environments and biomass burning plumes, and nighttime reactions with NO₃• (Atkinson and Arey, 2003; Ziemann and Atkinson, 2012). Due to strong activation by the -OCH₃ group, anisole can undergo rapid electrophilic addition and aromatic substitution reactions with OH• and NO₃• (Coeur-Tourneur et al., 2010; Lauraguais et al., 2016). Experimental and theoretical studies have determined reaction rate constants for anisole with OH• (2.86 \times 10^{-11} cm³ molecules⁻¹ s⁻¹), O₃ (2.64 \times 10⁻²¹ cm³ molecules⁻¹ s⁻¹), and NO₃• (9.45 \times 10⁻¹⁷ cm³ molecules⁻¹ s⁻¹) (Coeur-Tourneur et al., 2010; Lauraguais et al., 2016; Sun et al., 2016). These rate constants are comparable with phenol, methyl-phenols, and methoxy-phenols, but higher than those for other single-ring aromatic hydrocarbons, such as benzene, toluene, and xylene (Coeur-Tourneur et al., 2010; Lauraguais et al., 2016). Recent studies have highlighted the SOA yield and the formation of light-absorbing and redox-active products from anisole-related VOCs during atmospheric transport (Laskin et al., 2015; Liu et al., 2015; Tuet et al., 2017). For example, families of benzene and phenol species generate substantial brown carbon (BrC) aerosols via photooxidation in the presence or absence of NO_x and from nighttime NO₃• reactions in the atmosphere (Lin et al., 2015; Mayorga et al., 2021). The SOA generated from these reactions can induce adverse health effects upon inhalation, causing inflammation, oxidative stress, and genotoxicity (Chowdhury et al., 2019; Jiang et al., 2016; Tuet et al.,

2017). Oxidative potential (OP), which weighs the capability of particles to generate reactive oxygen species (ROS), is thought to be a reliable indicator of intrinsic particle toxicity (Bates et al., 2019; Zhang et al., 2022). The relatively high OP of SOA generated from benzene-family precursors has been emphasized (Jiang et al., 2016, 2017). However, the OP and cytotoxicity of SOA from phenolic compound precursors were seldomly characterized (Li et al., 2022). In addition, NO_x in polluted air can significantly modify atmospheric reactions and the composition of SOA. Yet, there are limited studies investigating the effect of NO_x levels on SOA toxicity, and no consensus on the impact has been drawn (Chowdhury et al., 2019; Tuet et al., 2017). Moreover, different chemical results for SOA from photooxidation and nighttime evolution have been reported, highlighting the importance of the diel process rather than aging by just a single pathway in describing SOA properties (Li et al., 2020). The roles of nighttime NO₃• aging and diel processes in modifying aerosol toxicity have not been investigated. These hinder our understanding of the dynamic transformations and impacts of these SOA during their atmospheric transport.

In short, anisole is a model pyrolysis pollutant and proxy of phenolic VOCs, but the atmospheric transformation of anisole and associated health effects were not studied. To fill the gap, this study employs a tandem-flow reactor system to simulate diel atmospheric aging of anisole, including daytime photooxidation in the presence of varying NO_x levels and subsequent nighttime NO_3 • reactions. The generated SOA were comprehensively characterized to determine the SOA yield, composition, OP, and cytotoxicity regarding diverse aging degrees and pathways. Moreover, potential health impacts induced by anisole SOA were estimated given these simulated atmospheric cycles.

2. Experiments and methods

2.1. SOA generation

The experimental setting for the generation, collection, and characterization of anisole SOA are shown in Fig. S1In short, a tandem-flow reactor system containing a potential aerosol mass oxidative flow reactor (PAM-OFR) and a custom-designed aerosol flow tube reactor (AFR) were employed. The PAM-OFR provides an OH•-induced photo-oxidation environment, where OH• radicals are generated via external O₃ photolysis and subsequent reaction with water. The AFR sustains dark reactions with O₃ and NO₃•(He et al., 2021; Li et al., 2019b, 2020). About 250 ppbv anisole was introduced into PAM-OFR via gentle N₂ purging liquid precursor (99%, Sigma-Aldrich) immersed in a cold ethanol bath. Details are given in Text S1.

A series of experiments were conducted to probe the effects of various reaction pathways and oxidation degree on anisole SOA formation. These experiments include a. PAM-OFR based anisole photo-oxidation under a wide range of OH \bullet exposures (OH_{exp}, (0.1–1.9) × 10^{12} molecules cm $^{-3}$), that is 1–14 equivalent ambient photochemical oxidation days (EAD hereafter), assuming a daily average OH \bullet concentration of 1.5 × 10^6 molecules cm $^{-3}$ (Mao et al., 2009). b. NO_x-associated 2.0 EAD under various RO₂ \bullet +NO/RO₂ \bullet +HO₂ \bullet ratios in the range of 0–1.7, simulating SOA generation under varying photochemical pollution conditions. c. Further 1.0, 2.0, 5.0 EAD aging of anisole SOA

via NO₃• reactions that mimic nighttime processes. The experimental parameters are summarized in Table 1. Each experiment was repeated at least twice, and the averaged results are discussed.

The PAM-OFR operation parameters, such as OH_{exp} and $RO_2 \bullet + NO/RO_2 \bullet + HO_2 \bullet$, were determined using the latest Aerodyne OFR exposure estimator (edition V3.1). High purity N_2O (99.999%) was added to initiate photochemical aging under varying NO_x levels after OH_{exp} and UV light photon flux were pre-estimated by measuring the decay of coinjected SO_2 (Thermo SO_2 analyzer, Model 43i). For dark heterogeneous aging, $NO_3 \bullet$ was generated by mixing O_3 and $O_3 \bullet$ under dry conditions. O_3 and $O_3 \bullet$ exposures for anisole SOA were estimated using a chemical box model (Text S1, Tables S1–S2, and Figs. S2–S4). The results suggest that the AFR experiments simulated $O_3 \bullet$ exposure of anisole SOA to approximately $O_3 \bullet O_3 \bullet O_3$

2.2. SOA concentration and density

A series of O_3 -scrubbers, diffusion dryers, and charcoal denuders for the removal of ozone, moisture, and other gaseous pollutants were installed downstream of both the PAM-OFR and the AFR. The generated particles were size-scanned by an SMPS (classifier model 3080, DMA model 3081, CPC model 3775low, TSI) and density-characterized using an aerodynamic aerosol classifier (AAC, Cambustion, U.K.) coupled to another SMPS. Monodispersed particles selected by the AAC were further measured for their mobility distribution by the SMPS. The

particles' effective density was derived from the ratios of their aerodynamic and mobility sizes, assuming sphericity. Wall losses of the particles in the dual-flow reactor system were corrected, the details are provided in Text S1. Based on the particle size distribution and density, the SOA mass concentrations were calculated considering particle wall loss

2.3. Total particulate peroxide and oxidative potential measurement

Anisole SOA generated from each run were collected onto PTFE filters (0.2 μm porosity, Omnipore) and processed immediately for offline analysis. Filters were vortex-shaking extracted twice in a total of 5 mL methanol (99.9%, Sigma-Aldrich). The extracts were filtered through PTFE membrane syringe filters (0.2 μm porosity, Millipore) and then pre-concentrated to 2.0 mL using a gentle flow of N_2 .

0.5 mL of the concentrated extract was withdrawn for measuring total particulate peroxide content (TPP, sum of $\rm H_2O_2$ and organic peroxides) using the iodometric-spectrophotometric method of Wang et al. (2021, 2018). Detailed method description and calibration curves are given in Text S2 and Fig. S5, respectively. In addition, the peroxide extraction efficiency was assessed (Text S2), and an average recovery rate of 94.8 \pm 2.2% was used to calibrate all extracts.

The total OP was assessed with the acellular dithiothreitol (DTT) assay adapted from Lin and Yu (2019). Specifically, 0.5 mL of the concentrated methanol extract was blown dry under a gentle $\rm N_2$ flow and reconstituted in 0.5 mL MiliQ water; then incubated with DTT (0.1 mM) in phosphate buffer solution (PBS, 0.1 M, pH 7.4, treated Chelex 100 Sodium form resin) openly at 37 °C. The pseudo-first-order DTT depletion rate was tracked spectrophotometrically (see details in Text

Table 1 Experiment and setup parameters.

Experiment	SOA (EAD)	PAM-OFR ₂₅₄							Aerosol flow reactor				
		OH _{exp} (molecules cm ⁻³ s)	O ₃ (ppm)	N ₂ O	RH	Photon flux (photon cm ⁻² s ⁻¹)	RT (s)	RO ₂ +NO/ RO ₂ +HO ₂	NO ₃ exp (molecules cm ⁻³ s)	O ₃ (ppm)	NO (ppm)	RH	RT (s)
OH* photochemical aging	1.0	1.3×10^{11}	44.6 ± 0.2	-	38.5 ± 0.3%	5.5×10^{13}	189	_	-	<5 ppb	0	<0.5%	-
	2.0*	2.6×10^{11}	$\begin{array}{c} 44.6 \\ \pm \ 0.2 \end{array}$	-	38.5 ± 0.3%	1.5×10^{14}	189	-	-	<5 ppb	0	<0.5%	-
	5.1	6.6×10^{11}	$\begin{array}{c} 44.6 \\ \pm \ 0.2 \end{array}$	-	38.5 ± 0.3%	5.4×10^{14}	189	-	-	<5 ppb	0	<0.5%	-
	10.2	1.3×10^{12}	$\begin{array}{c} 44.6 \\ \pm \ 0.2 \end{array}$	-	38.5 ± 0.3%	1.3×10^{15}	189	-	-	<5 ppb	0	<0.5%	-
	14.4	1.9×10^{12}	$\begin{array}{c} 44.6 \\ \pm \ 0.2 \end{array}$	-	38.5 ± 0.3%	2.0×10^{15}	189	-	-	<5 ppb	0	<0.5%	-
NO _x -involved photooxidation	2.2 (low- NO _x)	2.9×10^{11}	$\begin{array}{c} 45.3 \\ \pm \ 0.2 \end{array}$	0.5 vol %	39.3 ± 0.2%	1.1×10^{14}	189	0.01	-	<5 ppb	0	<0.5%	-
	2.2 (medium- NO _x)	2.9×10^{11}	$\begin{array}{l} 45.3 \\ \pm \ 0.2 \end{array}$	2.0 vol %	39.3 ± 0.2%	4.5×10^{14}	189	0.17	-	<5 ppb	0	<0.5%	-
	2.1 (high- NO _x)*	2.7×10^{11}	$\begin{array}{c} 45.3 \\ \pm \ 0.2 \end{array}$	4.0 vol %	39.3 ± 0.2%	1.9×10^{15}	189	1.68	-	<5 ppb	0	<0.5%	-
NO [*] 3 dominated- heterogeneous reaction	1.0	1.3×10^{11}	$\begin{array}{c} 44.8 \\ \pm \ 0.3 \end{array}$	-	38.9 ± 0.2%	5.5×10^{13}	189	-	1.03×10^{13}	$\begin{array}{c} 10.5 \\ \pm \ 0.2 \end{array}$	$\begin{array}{c} 6.3 \; \pm \\ 0.1 \end{array}$	<0.5%	227
	2.1*	2.7×10^{11}	$\begin{array}{c} 44.8 \\ \pm \ 0.3 \end{array}$	-	38.9 ± 0.2%	1.5×10^{14}	189	-	1.01×10^{13}	$\begin{array}{c} 10.5 \\ \pm \ 0.2 \end{array}$	$\begin{array}{c} 6.3 \; \pm \\ 0.1 \end{array}$	<0.5%	227
	5.2	6.7×10^{11}	$\begin{array}{c} 44.8 \\ \pm \ 0.3 \end{array}$	-	38.9 ± 0.2%	5.4×10^{14}	189	-	1.01×10^{13}	$\begin{array}{c} 10.5 \\ \pm \ 0.2 \end{array}$	$\begin{array}{c} 6.3 \; \pm \\ 0.1 \end{array}$	<0.5%	227

Note: * samples for ESI-HRMS analysis.

S3). After blank correction, the rate normalized by SOA mass concentration in the extract yields a value of OP_{SOA}^{DTT} (pmol min⁻¹ μ g⁻¹). In all experiments, less than 25% of DTT was consumed during incubation.

The OP for operational blank and for 1,4-naphthoquinone (1,4-NQ, 97%, Sigma-Aldrich) and standard peroxides as positive controls were measured frequently to ensure the reliability and consistency of the DTT assay (Text S3, Fig. S6). The measured OP for 1,4-NQ is 3.8 nmol min $^{-1}$ µg $^{-1}$, comparable to literature values (Jiang et al., 2017; Lin and Yu, 2019). Standard peroxides have an average OP of 3.14 pmol min $^{-1}$ nmol $^{-1}$. The results are consistent with data from Jiang et al. (2017) and Wang et al. (2018), considering the method differences in the DTT assay (Lin and Yu, 2019).

The light absorption of anisole SOA extracts in methanol was also measured at a wavelength range of 250–550 nm. The solution absorbance-based mass absorption cross section (MAC, m^2 g^{-1}) and imaginary part of the refractive index were calculated.

2.4. Chemical characterization

HR-Tof-AMS operating alternatively in V and W mode was used to monitor the bulk aerosol compositions in terms of organic fragments $(C_xH_y^+, C_xH_yO_i^+, C_xH_yO_i^+, C_xH_yO_iN_p^+, \text{and }NO_y^+, \text{where } x, y, z, p \geq 1, i \geq 0)$ and elemental ratios (O/C, H/C, and N/C) (Canagaratna et al., 2015).

Additionally, anisole SOA generated from 2.0 EAD under i) pristine OH• oxidation, ii) high level NO_X -involved OH• oxidation, and iii) nighttime NO_3 •-aging were collected for offline molecular analysis. A high-performance liquid chromatography (HPLC) column interfaced with a photodiode array (PDA) detector and with a high-resolution mass spectrometer (HRMS) equipped with an electrospray ionization source operated in negative mode (ESI(-)) was used to separate the components by polarity and characterize the eluted molecules. The HPLC-PDA-HRMS procedures follow Misovich et al. (2021) and the MS data processing method refers to Roach et al. (2011). More detailed information of HRMS analysis and data processing can be found in Text S4–S5. In this study, only results derived from the whole spectra over the entire retention time of HPLC-ESI(-)-HRMS analysis were discussed.

2.5. Cytotoxicity of anisole SOA

Four kinds of anisole SOA, generated from 2.0 EAD under i), ii), iii) conditions and 10.0 EAD (iv), were collected for cytotoxicity tests. Following the methanol extraction, the final SOA were reconstituted into DI water. A549 (ATCC® CCL-185 $^{\text{TM}}$ cell line) human lung epithelial cells were exposed to 150 and 300 mg L $^{-1}$ extracts for 5 h. As a control, operational-blank extracts were used. The DNA-intercalating dye propidium iodide (PI) was used to assess cell viability. Cellular ROS were measured using 2',7'-dichlorodihydrofluorescein diacetate (H₂DCFDA, Thermo Fisher Scientific) probe. The assays were performed using flow cytometry (Amnis® CellStream® Flow Cytometer, Luminex, US). Detailed information and statistical analysis are provided in Text S6.

3. Results and discussion

3.1. SOA yield

SOA yield is an important parameter in evaluating the atmospheric implication of VOCs. Unlike traditional anthropogenic species, SOA yields and oxidation mechanisms for anisole and many analog oxygenated chemical products are rarely investigated (Humes et al., 2022). In this study, no particle formation was measured from the homogeneous ozonolysis or NO₃• oxidation of gas-phase anisole, due to low reactivity and the high volatility of the products (Lauraguais et al., 2016; Sun et al., 2016). In contrast, OH• photooxidation of anisole generated particles with dehydrated densities of 1.3–1.4 g cm⁻³. According to the AMS results, all the particles generated were organic. As shown in Figs. S3A–C

and Fig. 1A, the mean sizes and average densities of anisole SOA steadily increased upon prolonged photochemical aging and subsequent NO₃• reactions, demonstrating that both extended photooxidation and nighttime aging facilitate particle growth and enlarge particle density.

Although the VOC was not directly monitored, the reacted anisole concentrations in the PAM-OFR were estimated based on the known OH_{exp} and OH_{\bullet} -reaction kinetics (see the detailed method in Text S1). Employing particle density, wall-loss corrected SOA, and reacted anisole concentrations, the SOA yields were estimated. It is noteworthy that these SOA yields can be underestimated compared to the actual atmospheric processes. The short residence time in the PAM-OFR may limit gas-particle partition, and the high oxidant concentration may lead to SOA fragmentation (Bruns et al., 2015; Lambe et al., 2011). Despite the inherent technical limitations, the calculated yields still provide insights into SOA formation ability by anisole under diverse aging conditions.

As presented in Fig. 1B and Table 2, the anisole SOA yield as a function of OH_{exp} reached a maximum of 0.34 at about 5.0 EAD, in agreement with SOA yields from numerous biogenic and anthropogenic VOCs (Lambe et al., 2012; Liu et al., 2019; Zhao et al., 2021). It is suggested that functionalization and gas-phase condensation lead to an initial increase in SOA yield with photooxidation. In contrast, further heterogenous OH_{\bullet} reactions lead to fragmentation of highly-oxygenated products, resulting in SOA loss.

Generally, NO_x alters both $RO_2 \bullet$ and $OH \bullet$ balance and modifies reaction channels through $NO_x/HO_x \bullet$ chemistry, thereby impacting SOA yields (Humes et al., 2022). Here, the $OH \bullet$ concentration (or OH_{exp}) was roughly maintained to isolate the effect of NO_x on SOA generation. It was found that anisole SOA generation was promoted by low NO_x levels but inhibited at higher NO_x levels. These findings agree with previous reports of SOA yield reduction with increasing $RO_2 \bullet + NO$ reactions for small molecular precursors (e.g., benzene, toluene, and monoterpenes), as NO_x interferes with autooxidation pathways, forms higher volatility products, and suppresses new particle formation and growth (Borrás and Tortajada-Genaro, 2012; Liu et al., 2019; Qi et al., 2020; Sarrafzadeh et al., 2016; Zhao et al., 2018).

Nighttime NO $_3\bullet$ reactions insignificantly (p < 0.05) increased the mass of daytime-generated anisole SOA, especially for the less photochemically-aged SOA. It is noted that the yield enhancements resulted from dark reactions between particles and NO $_3\bullet$, as the charcoal denuders removed gaseous anisole photochemical products. Nevertheless, the general mass increase demonstrates that functionalization occurred in anisole SOA, with a more significant mass addition for fresher SOA, indicating that fresher SOA has a higher reactivity towards NO $_3\bullet$.

3.2. Bulk SOA composition

According to the bulk aerosol chemical features presented in Fig. 2 and Fig. S7, photochemically-generated anisole SOA are highly oxygenated even at 1.0 EAD. The mass spectra resemble features of more oxidized oxygenated organic aerosol (MO-OOA) and methoxyphenol SOA (Chhabra et al., 2011; Li et al., 2014). In Fig. 2A, the higher H/C (≥ 1.34) and O/C (≥ 0.98) ratios of anisole SOA compared with its precursor (C7H8O) demonstrate hydrogen and oxygen additions to the particle-phase products. From Fig. 2A–B, extending $OH\bullet\mbox{ oxidation}$ steadily increased the O/C ratio and f44 (carboxyl fragment fraction). In contrast, the H/C ratio decreased, thus increasing the carbon oxidation state ($\overline{OS_C} = 2 \times O/C-H/C$) progressively from 0.51 to 1.31 after about equivalent two weeks of ambient photochemical oxidation. The carbonyl fragment composition (f43) first increased slightly, then gradually decreased after 2.0 EAD. The highest f43 and corresponding f44 are 2.0% and 17.6%, respectively. These changes indicate the generation of carboxyl products, while the minor carbonyl products are more favored at lower OH_{exp} . The changes in characteristic $C_xH_y^+$ fragments, e.g., $C_2H_2^+$, $C_4H_2^+$, $C_5H_5^+$, $C_6H_5^+$, etc., indicate possible

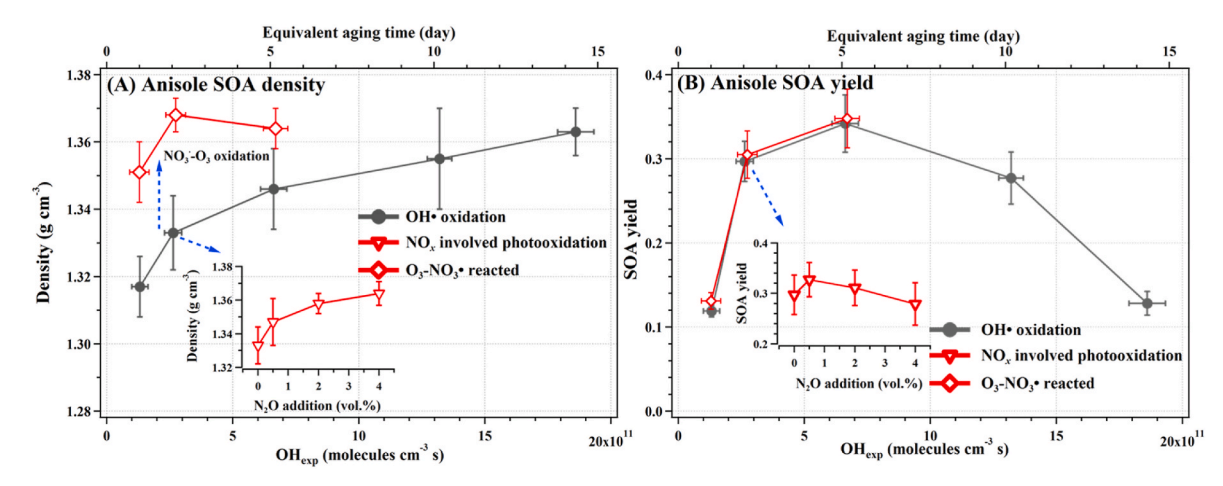


Fig. 1. Anisole SOA average density (A) and yield (B) for various reaction pathways and aging degrees. Pristine OH• oxidation is denoted by the solid gray circles, NO_x -involved photochemical reactions are displayed in the inserted graph by open red triangles, and NO_3 • heterogeneous aging is marked by the red-diamonds. (For interpretation of the references to color in this figure legend, the reader is referred to the Web version of this article.)

Table 2

Experiment	Anisole SOA (EAD)	Density (g cm ⁻³)	SOA yield	\overline{MAC} (m ² g ⁻¹)	OP_{SOA}^{DTT} (pmol min ⁻¹ μ g ⁻¹)	Total Peroxides (nmol μg^{-1})	
OH• photochemical aging	1.0	1.32 ± 0.01	0.119 ± 0.007	0.20 ± 0.06	64.3 ± 5.1	0.73 ± 0.06	
	2.0	1.33 ± 0.01	0.297 ± 0.024	0.15 ± 0.04	56.2 ± 2.4	0.32 ± 0.04	
	5.1	1.35 ± 0.01	0.342 ± 0.034	0.11 ± 0.03	39.2 ± 7.1	0.26 ± 0.05	
	10.2	1.36 ± 0.02	0.277 ± 0.031	0.07 ± 0.04	30.8 ± 2.9	0.26 ± 0.05	
	14.4	1.36 ± 0.01	0.128 ± 0.014	0.05 ± 0.01	22.2 ± 4.7	0.22 ± 0.06	
NO_x -involved photooxidation	2.2 (low-NO _x)	1.35 ± 0.01	0.327 ± 0.034	0.27 ± 0.04	44.6 ± 3.4	0.19 ± 0.04	
	2.2 (medium- NO_x)	1.36 ± 0.01	0.311 ± 0.035	0.33 ± 0.05	41.3 ± 4.1	0.15 ± 0.04	
	2.1 (high- NO_x)	1.36 ± 0.01	0.273 ± 0.039	0.52 ± 0.05	35.5 ± 1.9	0.10 ± 0.02	
NO [*] dominated-heterogeneous reaction	1.0	1.35 ± 0.01	0.131 ± 0.010	0.28 ± 0.05	73.9 ± 4.6	0.90 ± 0.09	
	2.1	1.37 ± 0.01	0.305 ± 0.028	0.22 ± 0.04	59.4 ± 4.4	0.36 ± 0.07	
	5.2	1.36 ± 0.01	0.349 ± 0.035	0.14 ± 0.03	40.5 ± 3.7	$\textbf{0.28} \pm \textbf{0.06}$	

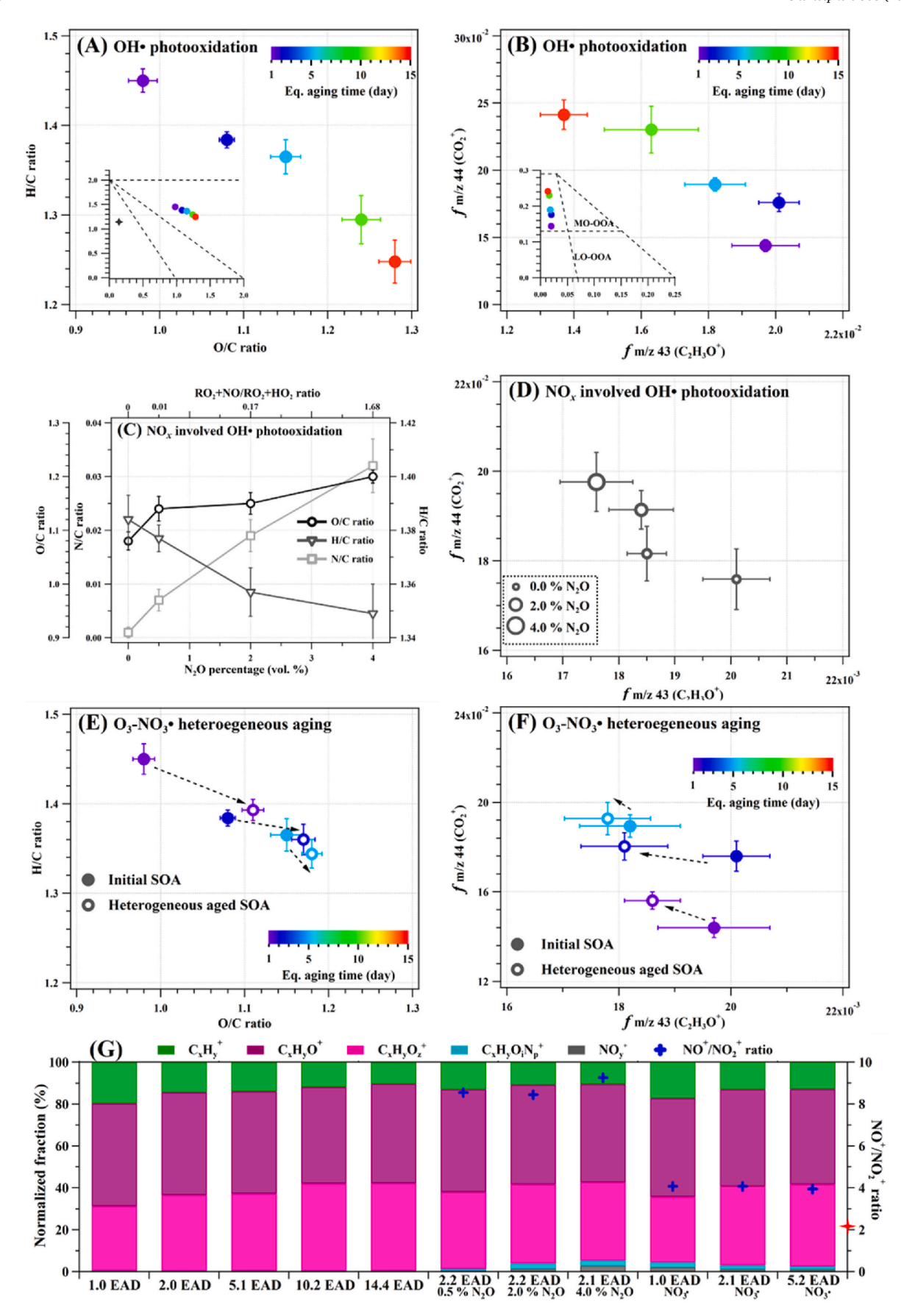
Note: mean \pm standard deviation; $\overline{\textit{MAC}}$ is wavelength (300–400 nm) weighted average mass absorption cross-section.

benzene-ring retention by reactions. As shown in Fig. S8, the summed aromatic hydrocarbon fractions (f_{Ar}) contributed less than 3.5 wt% in all anisole SOA. They diminished gradually with OH• oxidation, indicating that ring-cleavage and benzene-ring functionalization constitute an important reaction pathway in the photochemical transformations of anisole.

As shown in Fig. 2G, photooxidation in the presence of NO $_x$ produced nitrogen-containing fragments ($C_xH_yO_iN_p^+$) in anisole SOA. The higher characteristic NO $^+$ /NO $_2^+$ ratio (\sim 8.8 > 2.1 for standard ammonium nitrate particles) suggests organonitrate or/and nitroaromatic generation in anisole SOA under all NO $_x$ regimes (Li et al., 2019a, 2019b). With identical OH $_{exp}$, increasing the weight of RO $_2$ •+NO reaction pathway leads to higher nitrogen content and \overline{OS}_C , accompanied by noticeable f44 increase and minor f43 decrease in anisole SOA (Fig. 2C–D). The elevated NO $_x$ levels suppressed both particulate carboxy- and carbonyl production and the overall SOA yield.

Typically, NO₃• oxidation enhanced the $\overline{OS_C}$ and increased f44 and organic nitrate content in the aged anisole SOA (Fig. 2E–G). Yet, the

different NO⁺/NO₂⁺ ratios (4.0 on average) indicate different nitrate speciation between nighttime aging and photochemistry in a polluted environment. In addition, upon identical NO3• exposure, more pronounced chemical changes were observed for fresher photochemicallygenerated SOA, further confirming that fresh photochemicallygenerated anisole SOA is more reactive towards NO3. Kroll et al. (2009) reported that SOA mass following different levels of heterogeneous oxidation is governed by varying weights of functionalization (polar, oxygen-containing functional group $\bar{\text{addition}}$ and fragmentation (C-C bond cleavage). By combining the SOA yields and AMS results (Fig. S7), the elemental composition of NO₃•-aged anisole SOA were quantitatively analyzed. The mass increase for 1.0 EAD anisole SOA is attributed to mostly oxygen and less nitrogen addition while maintaining a constant carbon content. For 2.0 and 5.0 EAD SOA, evident carbon loss was observed following nighttime aging, while the overall insignificant mass change was due to a balance of functionalization and fragmentation. These results are consistent with Kroll et al. (2009) and also indicate that fragmentation of highly oxidized SOA occurs in diel



(caption on next page)

Fig. 2. AMS-based chemical evolution for anisole SOA through diverse atmospheric reactions. (A)–(B) The elemental ratio and specific fragment changes as a function of OH_{exp} . The black star symbol in the inserted graph in Figure A indicates the elemental characteristics of the anisole precursor. The dashed triangular region represents the ambient oxygenated organic aerosol (OOA), less-oxidized OOA (LO-OOA), and more-oxidized OOA (MO-OOA), mainly found in the lower and upper parts of the triangular region. (C)–(D) NO_x -associated photooxidation of anisole. (E)–(F) Heterogeneous reactions between photochemically-generated anisole SOA and NO_3 • under dark. (G) Overall fragment fractions and NO^+/NO_2^+ ratios (blue cross) for various anisole SOA. The red star on the right axis denotes NO^+/NO_2^+ ratio of 2.1 for standard dehydrated ammonium nitrate particles. (For interpretation of the references to color in this figure legend, the reader is referred to the Web version of this article.)

reaction pathways, for example, when switching from $OH \bullet$ photochemical aging to nighttime reactions with $NO_3 \bullet$.

3.3. Molecular characterization of SOA

The ESI(–)-HRMS spectra acquired from samples i (pristine OH• photooxidation), ii (high-level NO_X -involved photooxidation) and iii (NO_3 •-dominated heterogeneous oxidation) are displayed in Fig. S9. The characteristics of the assigned neutral molecular species based on the detected deprotonated ions are summarized in Fig. 3. Overall, the anisole SOA contains highly-oxygenated low molecular weight species with relatively low volatility. As shown in Fig. 3A–C, the major identified individual compounds have an O/C ratio of 0.5–1.5. Their intensity-weighted average O/C values are 1.06 (i), 1.12 (ii), and 1.09 (iii). The O/C values align with the AMS results, demonstrating that NO_X and NO_3 •

reactions increase the O/C ratio and $\overline{OS_C}$ of SOA. More abundant nitrogen-containing species (CHON) were identified in ii and iii samples (Fig. S9), indicating more nitrogen-containing products in high-NO_x photochemistry and NO3• reactions with anisole SOA. To infer the molecular characteristics of anisole SOA, intensity-weighted average molecular formulas were calculated. Because the ESI(-)-HRMS has varying sensitivity to CHO and CHON species, the intensity-weighted average molecular formulas of CHO and CHON species were calculated separately. The ensemble average molecular formula of each SOA was estimated using the AMS-derived N/C ratios (Text S5, Table S3). molecular formulas of $C_{5.99}H_{8.02}O_{6.08}N_{0.02}$ $C_{5\cdot 77}H_{7\cdot 76}O_{6\cdot 16}N_{0.18},$ and $C_{5\cdot 81}H_{7\cdot 74}O_{6\cdot 0}N_{0.12}$ were calculated for SOA corresponding to i, ii, and iii experiments, respectively. The general low carbon (\sim 6) and high oxygen values (\geq 6) suggest extensive cleavage of benzene rings and abstraction of methoxy groups in SOA formation

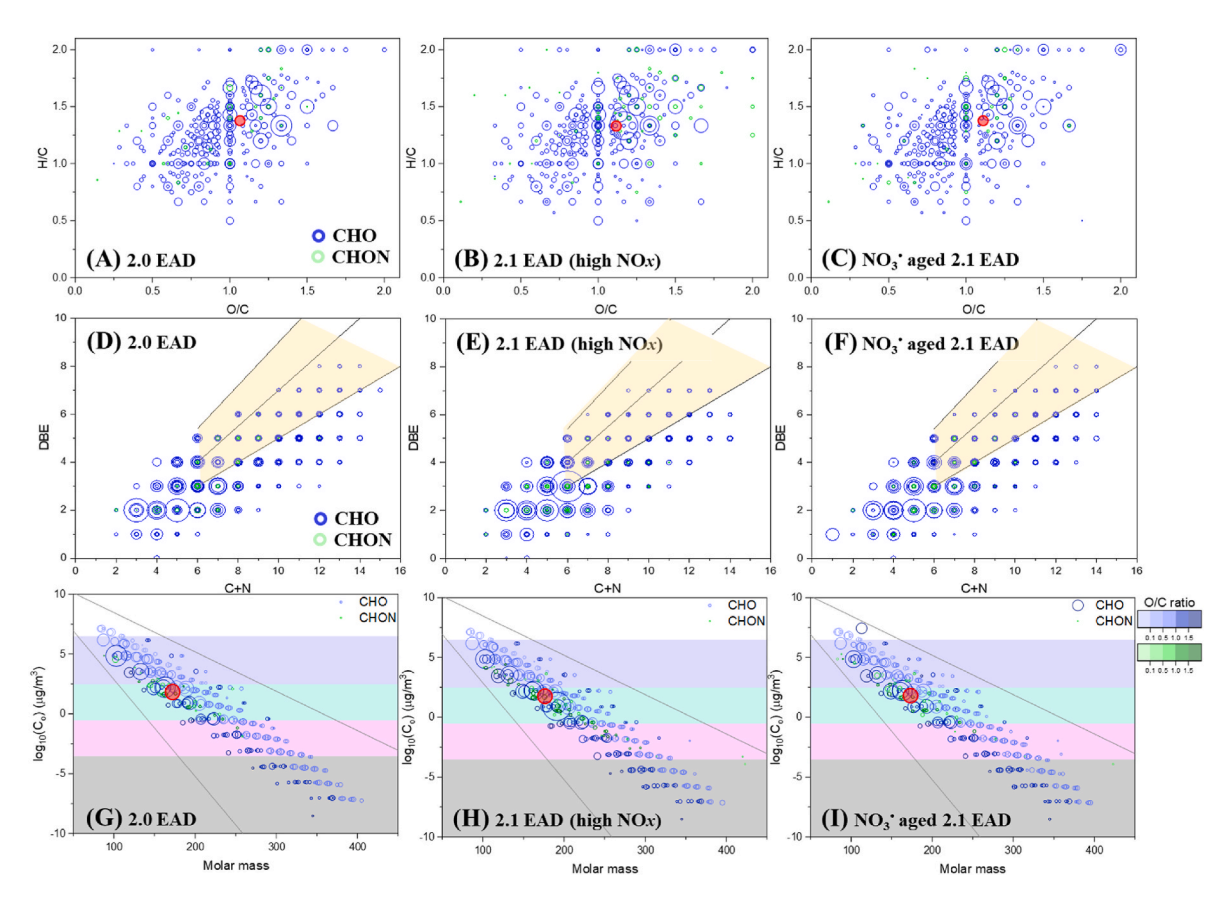


Fig. 3. (A)–(C) Van Krevelen plot of elemental ratios, (D)–(F) plot of double bond equivalent values (DBE = C + 1 - H/2 + N/2) vs. carbon and nitrogen numbers, (G)–(I) the molecular corridor of saturation mass concentration (C_0) in a logarithmic scale vs. molar mass of anisole SOA produced by various reaction pathways, including equivalent ambient two days' OH• photooxidation in the absence of NO_x, in the presence of high-level NO_x (4 vol% N₂O), and followed by dark NO₃• radical heterogeneous reactions. Intensity-weighted average elemental ratios are marked as red circles in panels A–C. Three referential lines in panels D–F, from bottom to top, represent linear polyenes C_xH_{x+2} , cata-condensed PAHs, and fullerene-like hydrocarbons, respectively (Lin et al., 2018). The light-yellow shaded region constrains potential BrC chromophores. The lines in panels G–I indicate reference values for linear alkanes C_nH_{2n+2} (upper with O/C = 0) and sugar alcohols $C_nH_{2n+2}O_n$ (lower with O/C = 1); five distinct regions are presented based on molecular volatility (from top to bottom: white for volatile organic compounds (VOCs), blue for intermediate-volatility OCs (IVOCs), green for low semi-volatility OCs (SVOCs), red for Low-Volatility OCs (LVOCs), and gray for extremely-low volatility OCs (ELVOCs) (Li et al., 2016). The circles represent individual compounds color-coded by O/C ratio for families of CHO and CHON. The size of the circles is scaled by the cubic root of the MS signal intensity. Intensity-weighted average molecular weight and corresponded volatility are marked as red circles in panels G–I. (For interpretation of the references to color in this figure legend, the reader is referred to the Web version of this article.)

reactions. These observations are consistent with the AMS data showing very low intensities of aromatic hydrocarbon fragments in anisole SOA (Fig. S8). The slight decrease in C and H and the increase in N averaged values in the ii and iii samples (compared to i) further support fragmentation, hydrogen-abstraction, and nitrogen addition. Less significant formula differences between samples i and iii indicate that NO₃• nighttime reactions are only modestly important for 2.0 EAD SOA, while NO_x-involved photochemical reactions modify the composition of anisole SOA more substantially.

Information on the molecular structures of anisole SOA is further inferred from Fig. 3D-F, which depicts the DBE (double bond equivalent) versus the number of C + N atoms corresponding to the identified species. The three reference lines indicate the limits of linear polyenes C_xH_{x+2} (DBE = 0.5 × C), cata-condensed PAHs (DBE = 0.75 × C - 0.5), and fullerene-like hydrocarbons (*DBE* = $0.9 \times C$) (Cain et al., 2014; Lin et al., 2018). Since light absorption requires an extended network of double bonds, SOA components with DBE/C ratios above the linear polyenes line may be potential BrC chromophores (Lin et al., 2018). Due to the relatively short carbon skeleton of the identified SOA species, modest BrC absorption by anisole SOA can be expected. Additionally, the NO_x-involved (ii) and the NO₃• dominated (iii) aging pathways may increase BrC absorption, as indicated by a larger amount of SOA products falling into the potential BrC chromophore region for those samples. These observations are verified by anisole SOA absorption. See optical results in Fig. S10 and calculated MAC in Table 2. OH• photooxidation of anisole can be a source of very weakly-absorbing BrC (Hettiyadura et al., 2021). Extensive OH• aging decreased the absorption ("bleached") of anisole SOA, while both NOx and NO3• reactions enhanced light absorption of generated SOA.

Volatility is important for determining organic compounds' gasparticle partitioning during atmospheric transport. The "molecular corridor" approach is commonly used to estimate the volatility of individual organic compounds quantified in terms of their saturation mass concentrations $(C_0, \mu g \ m^{-3})$ (Li et al., 2016). Fig. 3G–I presents the volatility of SOA components on a logarithmic scale (logC_0) as a function of molecular weight. Remarkably, the components of all anisole SOA samples span a broad range of intermediate ($C_0 \leq 3 \times 10^6 \ \mu g \ m^{-3}$) to extremely low ($C_0 \leq 3 \times 10^{-6} \ \mu g \ m^{-3}$) volatilities, while the most prominent species are semi-volatile (0.3 $< C_0 < 300 \ \mu g \ m^{-3}$). Intensity-weighted average C_0 was calculated to be 105, 59, and 100 $\mu g \ m^{-3}$, corresponding to anisole SOA from i, ii, and iii conditions, respectively. Photooxidation under high NO_x and nighttime $NO_3 \bullet$ reactions resulted in SOA with somewhat lower volatility, originating from more oxygenated products, as well as lower volatility nitro- and nitrate-organic products (Li et al., 2016).

3.4. Particulate peroxides and oxidative potential

Total particulate peroxides (TPP) content and oxidative potential (OP_{SOA}^{DTT}) for anisole SOA following atmospheric aging processes were quantified. As shown in Fig. 4A and B, a similar decreasing trend was observed for both TPP and OP_{SOA}^{DTT} with prolonged OH• photooxidation, and the robust exponential correlations were fitted:

$$TPP = 0.25 + 3.05 \exp\left(-\frac{OH_{exp}}{7.16 \times 10^{11}}\right)$$
 (1)

$$OP_{SOA}^{DTT} = 17.6 + 52.36 \exp\left(-\frac{OH_{exp}}{8.94 \times 10^{11}}\right)$$
 (2)

Notably, peroxides are photolabile under short wavelength UV light (Zawadowicz et al., 2020). Hence, TPP generation can be underestimated in a PAM-OFR equipped with 254 nm lamps. The fresh anisole SOA of 1.0 EAD has TPP of 0.73 nmol μg^{-1} (14.6 wt% assuming an average organoperoxide molecular weight of 200 m/z), it decreased

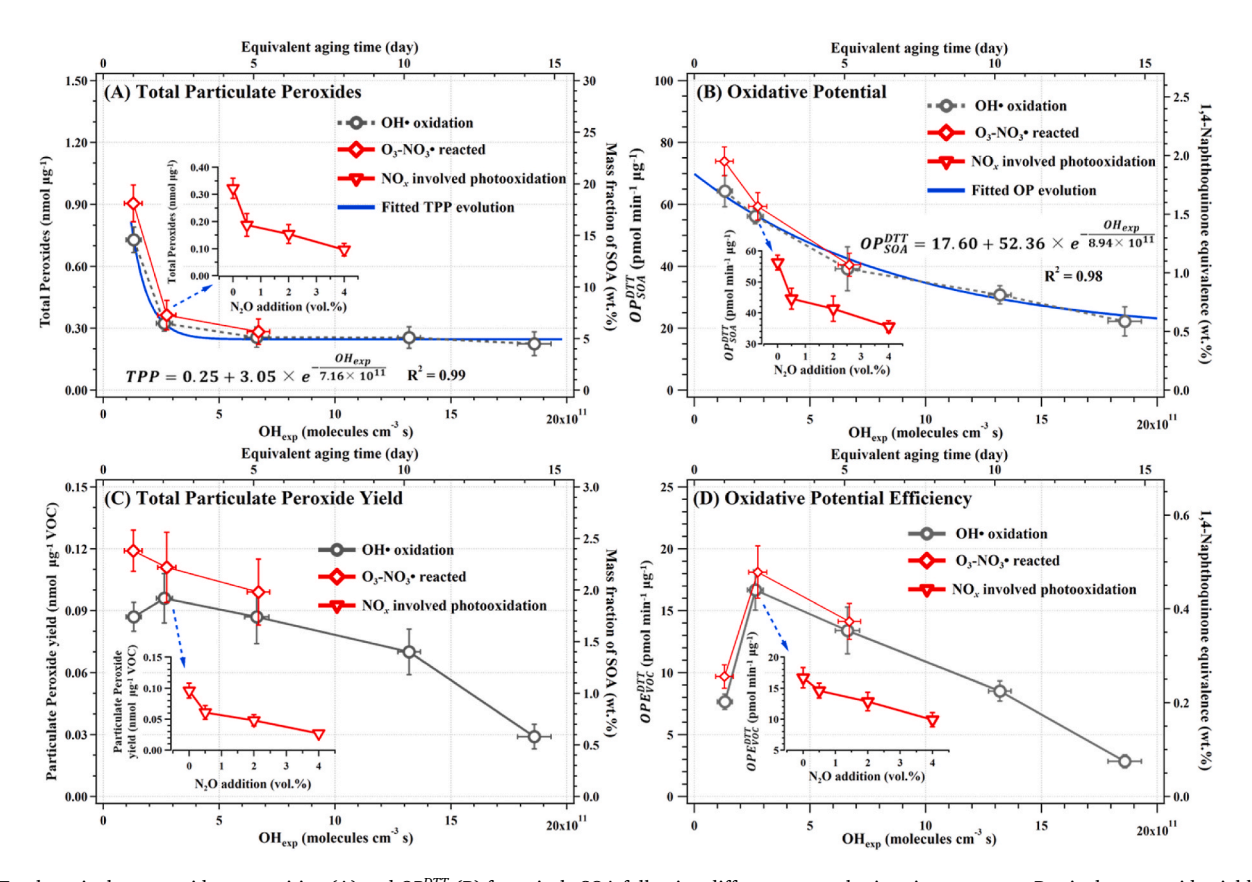


Fig. 4. Total particulate peroxide composition (A) and OP_{SOT}^{DTA} (B) for anisole SOA following different atmospheric aging processes. Particulate peroxide yield (C) and (D) particle-induced oxidative potential efficiency (OP_{VOC}^{DTA}) of anisole following atmospheric transformations.

sharply and leveled off after 2.0 EAD. Overall, the anisole SOA TPP contents are lower than those measured in biogenic SOA formed by photochemical processes (Chowdhury et al., 2019; Zhang et al., 2022). This suggests that the peroxide generation depends mainly on the VOC precursors, and anisole, like other phenolic and aromatic compounds (e. g., naphthalene, toluene, etc.), does not generate particulate peroxides efficiently (Sato et al., 2012; Wang et al., 2018).

Fresh anisole SOA has a OP_{SOA}^{DTT} of 64.3 pmol min⁻¹ μ g⁻¹, which is comparable to OP of smoke particles and other anthropogenic SOA (Jiang et al., 2020, 2017; Ma et al., 2021; Wang et al., 2018), but higher than the OP of biogenic SOA, such as isoprene and monoterpene-related SOA (Tuet et al., 2017). The decrease of anisole OP_{SOA}^{DTT} indicates the loss of redox-active composition as photooxidation progressed. Similar trends were observed for various anthropogenic and biogenic OA as their OP decreased after daytime photooxidation, attributed to the decomposition of organoperoxides, quinones, and electron-deficient alkenes that act as DTT consumers (Jiang et al., 2017; Jiang and Jang, 2018). These redox-active species can be photochemical products from numerous VOC precursors and are also susceptible to irradiation and reactions with OH• (Jiang et al., 2017; Jiang and Jang, 2018). These trends are also verified by the dominating ring-cleavage reactions and the measured decay of f_{Ar} (Fig. S8) and peroxides by photooxidation of anisole

The dependence of peroxide formation on NO_x concentration has been confirmed by Mertes et al. (2012) and Tuet et al. (2017). In this study, increasing NO_x levels under identical OH_{exp} suppressed TPP generation. Mertes et al. (2012) described similar observations for α-pinene SOA, where the measured peroxide composition decreased with photochemical oxidation and NOx concentration. RO2+HO2 represents the major peroxide formation pathway. Thus, with increasing NO_x concentration, additional competitive RO₂•+NO reactions reduce the peroxide generation. Anisole OP_{SOA}^{DTT} also decreased significantly with increasing NO_x levels. Specifically, under high NO_x conditions (4 vol% N_2O addition), the initial OP_{SOA}^{DTT} decreased by about 37% to 35.5 pmol $min^{-1}\ \mu g^{-1}.$ The NO_x effect on SOA OP depends mainly on the precursors and atmospheric aging. For example, Jiang et al. (2017) observed a sharp decrease of isoprene SOA OP with increasing NO_x concentration, while the OP values of toluene, 1,3,5-trimethylbenzene, and α-pinene SOA were more sensitive to the degree of photochemical aging than to NO_x levels. Nighttime NO₃• exposure resulted in significant TPP addition and OP enhancement to fresh anisole SOA of 1.0 EAD, likely due to the higher reactivity of fresh SOA to NO₃•.

Multiplying by SOA yield, TPP generation efficiency and total particle-induced OP (OPE_{VOC}^{DTT}) in the atmospheric transformation of anisole is proposed for the first time. In Fig. 4C, the TPP yield (0.096 nmol μg^{-1} gaseous anisole) via OH• photooxidation peaked at 2.0 EAD. Afterward, it gradually decreased. NO_x addition induces competing reactions between RO₂•+NO and RO₂•+HO₂•. In addition, the increased UV intensity needed to maintain consistent OH• concentrations in the PAM-OFR can decompose the peroxides synergistically. Altogether, the TPP yield decreased at higher NO_x levels. An enhanced TPP yield following nighttime NO₃• exposure was measured, especially for 1.0 FAD SOA

In Fig. 4D, the OPE_{VOC}^{DTT} of anisole SOA also peaked at 2.0 EAD, suggesting that 2 days of photooxidation in the atmosphere of anisole may pose the most severe oxidative hazard to human health. However, anisole OPE_{VOC}^{DTT} in photooxidation is suppressed by NO_x , demonstrating that atmospheric transformation/degradation of anisole in a polluted environment contributes less particulate oxidative hazard than that in a clean environment, because of the suppressed SOA yield and lowered OP_{SOA}^{DTT} . Following daytime photooxidation, nighttime $NO_3 \bullet$ aging in polluted environments may amplify the oxidative capacity of anisole SOA, especially when relatively fresh.

Based on the measured standard peroxide OP of 3.13 pmol min⁻¹ nmol⁻¹, the isolated contribution of anisole TPP to the measured OP_{SOA}^{DTT}

was tentatively estimated. As displayed in Fig. S11, TPP contributed less than 4% of OP_{SOA}^{DTT} for all samples, suggesting the substantial roles of nonperoxide redox-active species, such as quinones, electron-deficient alkenes, or/and other unidentified compounds. Similar results are found for photochemically-generated anthropogenic SOA; e.g., naphthalene SOA has a high OP_{SOA}^{DTT} (100–129 pmol min⁻¹ μ g⁻¹) with a derived peroxide contribution of less than 5% (Kautzman et al., 2010; Tuet et al., 2017; Wang et al., 2018), see literature comparison in Fig. 5. The V-shape of TPP contribution in anisole OP_{SOA}^{DTT} with OH_{exp} (Fig. S11) also appeared for toluene SOA photooxidation under low- OH_{exp} (Fig. S11) also appeared for wood smoke aging (Jiang and Jang, 2018), probably arising from different kinetics of peroxides and other redox-active compounds in reaction with $OH \bullet$. OH_{exp} heterogeneous reactions increase the peroxide contributions to anisole SOA OP, while OH_{exp} in daytime photochemistry has the opposite effect.

3.5. Anisole SOA cytotoxicity

Dose-dependent cell viability is observed when A549 cells were exposed to all types of anisole SOA, particularly for NOx involved (ii) and NO₃• reacted (iii) SOA (Fig. 6A). Out of all anisole SOA studied, 2.0 EAD SOA after nighttime aging induced the highest cell damage (approximately 20% of dead/damaged cells). The cytotoxicity, after exposure to 300 mg L⁻¹ SOA, follows the order: NO₃• aged 2.0 EAD SOA > high-NO_x 2.0 EAD SOA > 2.0 EAD SOA > 10.0 EAD (iii > ii > i > iv). For low dosage exposure of 150 mg L^{-1} , there are no significant differences (p < 0.05) in cell death induced by SOA apart from nighttime aged SOA (iii > i > iv > ivii). This trend indicates that nighttime NO₃• aging can significantly enhance the cytotoxicity of photochemically-generated SOA (p < 0.05), and that SOA generated in a polluted photochemical environment with a high NO_x level may be more toxic than SOA produced in a clean environment upon high exposure. Overall, NO_x has no statistically significant influence on SOA cytotoxicity, in agreement with previous studies on hydrocarbon precursors derived from SOA (Chowdhury et al., 2019). In contrast to hydrocarbon VOCs, such as naphthalene and α-pinene, where the aged SOA is more toxic than fresh SOA (Chowdhury et al., 2019; Zhang et al., 2022), extensive OH• photooxidation (10.0 vs. 2.0 EAD) did not lead to a significant change in cytotoxicity of anisole SOA.

In Fig. 6B, exposure to anisole SOA, except for the high-NO_x involved 2.0 EAD SOA, increased intracellular ROS (mainly H2O2) significantly (p < 0.05), but without a clear dose-response in ROS generation. The cell death results are consistent with the observed OPDTT trends and particulate peroxide content (Fig. 4); nighttime NO3•-processed SOA induced the strongest oxidative stress and the highest ROS contents in exposed cells. At the same time, exposure of high-NO_x involved SOA had the lowest ROS generation in lung cells. This highlights that both reaction pathways and the environmental pollutants can control SOA toxicity and demonstrates that cellular oxidative stress is an important mechanism of anisole SOA cytotoxicity, which agrees with findings for other SOA and biomass burning related aerosols (Chowdhury et al., 2019; Pardo et al., 2021, 2020). Similar to the cell death results, extensive photooxidation did not increase the oxidative stress of anisole SOA significantly, similar to ROS generation after exposure of the cells to fresh and aged SOA (2.0 vs. 10.0 EAD).

4. Conclusions and implications

This is the first comprehensive study on the atmospheric transformations of anisole (methoxybenzene, typical biomass pyrolysis VOC and proxy for VCPs) and the associated health effects following complex aging channels. We found that anisole may be an appreciable contributor to urban SOA, and its SOA yields rely on both reaction pathways and oxidation degree. Furthermore, consecutive diel aging and ambient pollution levels significantly modify SOA compositions and properties.

Homogeneous OH• photooxidation generates anisole SOA more

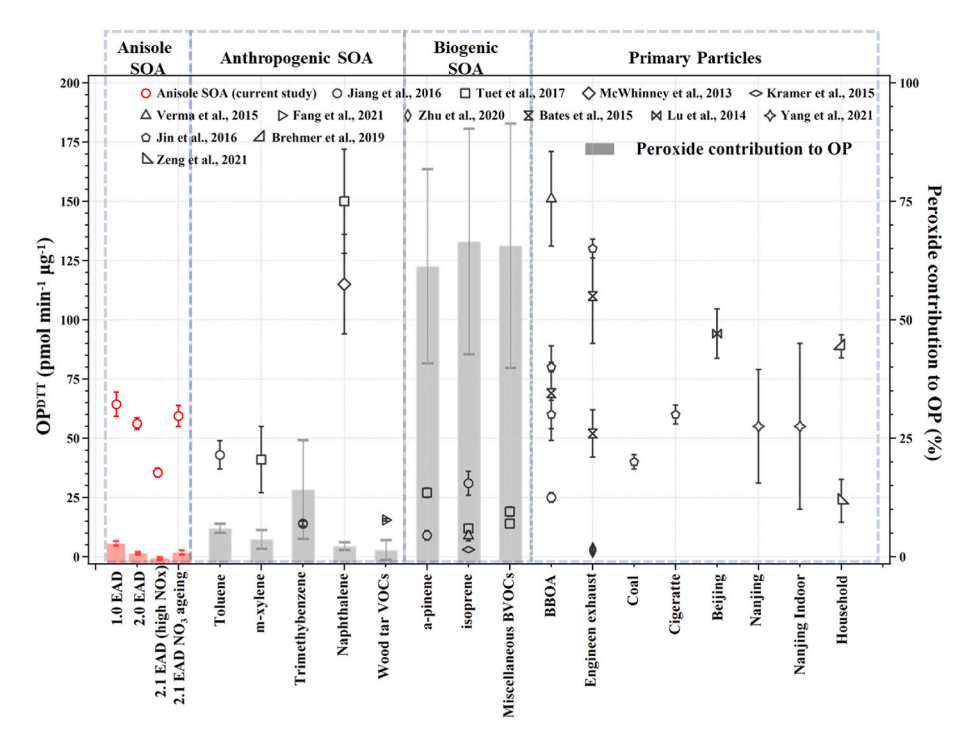


Fig. 5. Referential comparation of anisole OP_{SOA}^{DOT} with various particles from specific sources and environments (Bates et al., 2019; Bates et al., 2019; Fang et al., 2021; Jiang et al., 2016; Jiang et al., 2016; Kautzman et al., 2010; Li et al., 2014; Mertes et al., 2012; Tuet et al., 2017; Verma et al., 2015; Yang and Liu, 2021; Zhang et al., 2022; Zhu et al., 2020). Values of peroxide contribution to particle oxidative activity were derived from the relevant references (Kautzman et al., 2010; Mertes et al., 2012; Ma et al., 2021; Sato et al., 2012, Sun et al., 2016), assuming an average molecular weight of m/z-200 and an OP of 3.13 pmol min $^{-1}$ µg $^{-1}$ for organic peroxide.

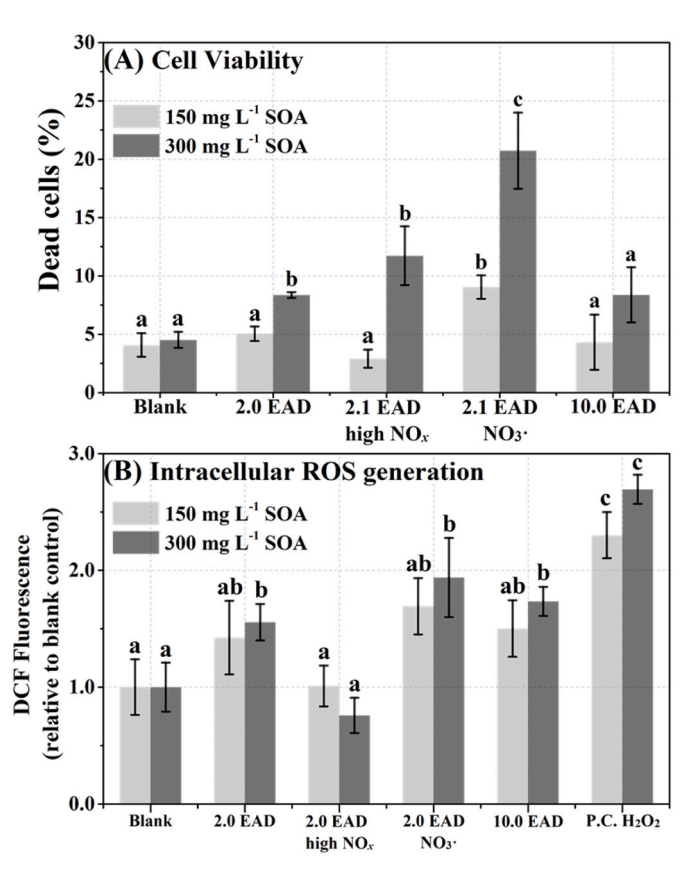


Fig. 6. Anisole-SOA is cytotoxic towards A549 lung cells. (A) Lung epithelial cells were exposed to 150 and 300 mg L $^{-1}$ anisole-SOA for 5 h. Cell cytotoxicity was determined by the intercalating PI dye. (B) Intracellular ROS generations after 5 h exposure at 150 and 300 mg L $^{-1}$. ROS were measured using H₂DCF-DA, detection was performed by flow cytometry. 100 μ M H₂O₂ was used as positive control (P·C.). The data represent the mean \pm SD. Mean values with different letters indicate significant differences at p < 0.05 using the Tukey HSD test. These experiments were performed in triplicate.

efficiently than O₃ or nighttime NO₃• reactions. The SOA yield (0.12–0.34) against pure OH• photooxidation varies with equivalent ambient aging time and is maximal after about 5 days in the clean air. Unlike typical biogenic and anthropogenic hydrocarbons (Chhabra et al., 2011; Sato et al., 2012; Tong et al., 2019), photochemically-generated anisole SOA consists of highly-oxygenated products with small molecular weight and low volatility that form via benzene-ring cleavage OH• reactions. Together with other phenols, methoxyphenols, and their derivatives (Chhabra et al., 2011; Yu et al., 2014), anisole is a precursor of highly oxygenated SOA in the urban environment and in biomass burning plumes, which can lead to reduced air quality and adverse health effects, considering the crucial role of highly oxygenated organic molecules in the air (Roldin et al., 2019; Tong et al., 2019).

Fresher anisole SOA are more absorbing and contain more organoperoxides and other redox-active entities to induce higher oxidative potential (OP_{SOA}^{DTT}). For example, anisole SOA generated from approximately 1.0 day of ambient photooxidation are very weakly-absorbing brown carbon aerosol (VW–BrC), which consist of 0.73 nmol organoperoxides μg^{-1} aerosol (14.6 wt%) with OP_{SOA}^{DTT} of 64.3 pmol min⁻¹ μg^{-1} , demonstrating that it can readily produce redox-active compounds and BrC shortly after anisole has been released in the atmosphere. Extensive OH• aging or longer residence/transport time in the atmosphere progressively enhances the oxidation state of anisole SOA but exponentially decreases the organoperoxide content, OP_{SOA}^{DTT} , and light absorption. Yet, fresh and aged anisole SOA maintain their high cytotoxicity and can induce oxidative damage to lung epithelial cells.

Considering the aging time/degree dependent SOA yield, we suggest that two days' photooxidation of anisole produces the most particle-bound organoperoxides; thus, it can pose the highest oxidative hazard (highest OP_{VOC}^{DTT}). With further photooxidation, the particulate organoperoxides and OP_{VOC}^{DTT} decrease steadily for up to two weeks of atmospheric transport. The time lag between anisole emission and highest organoperoxide yield and OP_{VOC}^{DTT} implicates relatively large-scale influences of anisole pollution, primarily affecting areas downwind from the emission source where ROS burden and particle-induced health impact could be enhanced due to photooxidation.

In polluted environments, NO_x alters anisole photochemical reaction

pathways by varying the importance of RO_2 reaction channels, modifying SOA generation and properties. Briefly, high NO_x levels suppress both SOA and organoperoxides yield, decrease particle OP_{SOA}^{DTT} , and enhance particle light absorption by generating nitrogen-containing chromophores. High NOx levels insignificantly influence anisole SOA cytotoxicity, but the SOA formed generate less ROS in exposed lung cells.

SOA generated during the daytime are subject to nighttime aging. Fresher photochemically-produced anisole SOA have higher susceptibility to react with NO3•. Overnight NO3• oxidation further increases the organoperoxide and organic nitrate content of anisole SOA, increasing SOA light absorption and OP_{SOA}^{DTT} . Most importantly, overnight aging significantly enhances cytotoxicity and oxidative stress potential of anisole SOA. In addition, the correlation between anisole OP_{SOA}^{DTT} , SOA exposure induced cellular ROS generation, and cell death rate demonstrates that oxidative stress is a key mechanism in anisole SOA cytotoxicity.

We know that SOA formation and evolution in the atmosphere are influenced by many additional factors, including varying oxidation environments, dispersion, and interactions with other pollutants during transport (Kroll and Seinfeld, 2008). By simply integrating laboratory-derived SOA yield and SOA normalized properties, this study provides novel insights into the dynamic products and impacts of gaseous precursors following atmospheric aging. Overall, this study shows that SOA formation from biomass burning VOCs increases the potential to induce adverse health effects for exposed populations away from the smoke origin. With the increasing frequency and intensity of fires due to global warming, biomass burning SOA in long-range transport of biomass burning smoke may be considered a health hazard in addition to the primary smoke particles. Moreover, air pollution and the diel-cycle-dependent anisole SOA properties call for additional investigations and considerations for depicting aerosol transformation and effects.

Supporting information

Texts S1-S6, Figs. S1-S11, and Tables S1-S3.

Declaration of competing interest

The authors declare that they have no known competing financial interests or personal relationships that could have appeared to influence the work reported in this paper.

Data availability

Data will be made available on request.

Acknowledgments

The study was partially supported by the Israel Science Foundation (ISF) (#3205/19), the Helmholtz Association, and the Weizmann Institute of Science in the framework of the German Israeli project "aero-HEALTH Helmholtz International Lab". YR acknowledges support by the research grant from the Anita James Rosen Foundation. YR, MVM and AL acknowledge support from the US National Science Foundation (Grant No. AGS-2039985/US-Israel Binational Science Foundation, BSF Grant No. 2020656). The authors thank Bill Brune for providing the PAM reactor. CL acknowledges support from the Planning & Budgeting Committee, Israel (2020/21), and especially from the VATAT fellowship.

Appendix A. Supplementary data

Supplementary data to this article can be found online at https://doi.

org/10.1016/j.chemosphere.2022.136421.

References

- Akinrinola, F.S., Darvell, L.I., Jones, J.M., Williams, A., Fuwape, J.A., 2014. Characterization of selected Nigerian biomass for combustion and pyrolysis applications. Energy Fuels 28, 3821–3832.
- Arivazhagan, M., Rexalin, D.A., Geethapriya, J., 2013. Vibrational spectra, DFT quantum chemical calculations and conformational analysis of P-iodoanisole. Spectrochim. Acta. A. Mol. Biomol. Spectrosc. 113, 236–249.
- Atkinson, R., Arey, J., 2003. Atmospheric degradation of volatile organic compounds. Chem. Rev. 103, 4605–4638.
- Bates, J.T., Fang, T., Verma, V., Zeng, L., Weber, R.J., Tolbert, P.E., Abrams, J.Y., Sarnat, S.E., Klein, M., Mulholland, J.A., 2019. Review of acellular assays of ambient particulate matter oxidative potential: methods and relationships with composition, sources, and health effects. Environ. Sci. Technol. 53, 4003–4019.
- Betancourt, D.A., Krebs, K., Moore, S.A., Martin, S.M., 2013. Microbial volatile organic compound emissions from Stachybotrys chartarum growing on gypsum wallboard and ceiling tile. BMC Microbiol. 13, 1–10.
- Borrás, E., Tortajada-Genaro, L.A., 2012. Secondary organic aerosol formation from the photo-oxidation of benzene. Atmos. Environ. 47, 154–163.
- Brown, S.S., Stutz, J., 2012. Nighttime radical observations and chemistry. Chem. Soc. Rev. 41, 6405–6447.
- Bruns, E.A., El Haddad, I., Keller, A., Klein, F., Kumar, N.K., Pieber, S.M., Corbin, J.C., Slowik, J.G., Brune, W.H., Baltensperger, U., 2015. Inter-comparison of laboratory smog chamber and flow reactor systems on organic aerosol yield and composition. Atmos. Meas. Tech. 8, 2315–2332.
- Cain, J., Laskin, A., Kholghy, M.R., Thomson, M.J., Wang, H., 2014. Molecular characterization of organic content of soot along the centerline of a coflow diffusion flame. Phys. Chem. Chem. Phys. 16, 25862–25875.
 Canagaratna, M.R., Jimenez, J.L., Kroll, J.H., Chen, Q., Kessler, S.H., Massoli, P.,
- Canagaratna, M.R., Jimenez, J.L., Kroll, J.H., Chen, Q., Kessler, S.H., Massoli, P., Hildebrandt Ruiz, L., Fortner, E., Williams, L.R., Wilson, K.R., 2015. Elemental ratio measurements of organic compounds using aerosol mass spectrometry: characterization, improved calibration, and implications. Atmos. Chem. Phys. 15, 253–272.
- Chen, J., Li, C., Ristovski, Z., Milic, A., Gu, Y., Islam, M.S., Wang, S., Hao, J., Zhang, H., He, C., Guo, H., Fu, H., Miljevic, B., Morawska, L., Thai, P., Lam, Y.F., Pereira, G., Ding, A., Huang, X., Dumka, U.C., 2017. A review of biomass burning: emissions and impacts on air quality, health and climate in China. Sci. Total Environ. 579, 1000–1034. https://doi.org/10.1016/j.scitotenv.2016.11.025.
- Chhabra, P.S., Ng, N.L., Canagaratna, M.R., Corrigan, A.L., Russell, L.M., Worsnop, D.R., Flagan, R.C., Seinfeld, J.H., 2011. Elemental composition and oxidation of chamber organic aerosol. Atmos. Chem. Phys. 11, 8827–8845.
- Chowdhury, P.H., He, Q., Carmieli, R., Li, C., Rudich, Y., Pardo, M., 2019. Connecting the oxidative potential of secondary organic aerosols with reactive oxygen species in exposed lung cells. Environ. Sci. Technol. 53, 13949–13958. https://doi.org/ 10.1021/acs.est.9b04449.
- Coeur-Tourneur, C., Cassez, A., Wenger, J.C., 2010. Rate coefficients for the gas-phase reaction of hydroxyl radicals with 2-methoxyphenol (guaiacol) and related compounds. J. Phys. Chem. A 114, 11645–11650.
- Fang, Z., Li, C., He, Q., Czech, H., Gröger, T., Zeng, J., Fang, H., Xiao, S., Pardo, M., Hartner, E., 2021. Secondary organic aerosols produced from photochemical oxidation of secondarily evaporated biomass burning organic gases: chemical composition, toxicity, optical properties, and climate effect. Environ. Int. 157, 106801.
- Fiege, H., Voges, H.-W., Hamamoto, T., Umemura, S., Iwata, T., Miki, H., Fujita, Y., Buysch, H.-J., Garbe, D., Paulus, W., 2000. Phenol derivatives. Ullmanns Encycl. Ind. Chem
- Fischer, G., Müller, T., Schwalbe, R., Ostrowski, R., Dott, W., 2000. Exposure to airborne fungi, MVOC and mycotoxins in biowaste-handling facilities. Int. J. Hyg Environ. Health 203, 97–104.
- Gilman, J.B., Lerner, B.M., Kuster, W.C., Goldan, P.D., Warneke, C., Veres, P.R., Roberts, J.M., De Gouw, J.A., Burling, I.R., Yokelson, R.J., 2015. Biomass burning emissions and potential air quality impacts of volatile organic compounds and other trace gases from fuels common in the US. Atmos. Chem. Phys. 15, 13915–13938.
- Hatch, L.E., Luo, W., Pankow, J.F., Yokelson, R.J., Stockwell, C.E., Barsanti, K.C., 2015. Identification and quantification of gaseous organic compounds emitted from biomass burning using two-dimensional gas chromatography-time-of-flight mass spectrometry. Atmos. Chem. Phys. 15, 1865–1899.
- He, Q., Tomaz, S., Li, C., Zhu, M., Meidan, D., Riva, M., Laskin, A., Brown, S.S., George, C., Wang, X., 2021. Optical properties of secondary organic aerosol produced by nitrate radical oxidation of biogenic volatile organic compounds. Environ. Sci. Technol. 55, 2878–2889.
- Hettiyadura, A.P.S., Garcia, V., Li, C., West, C.P., Tomlin, J., He, Q., Rudich, Y., Laskin, A., 2021. Chemical composition and molecular-specific optical properties of atmospheric Brown carbon associated with biomass burning. Environ. Sci. Technol. 55, 2511–2521.
- Humes, M.B., Wang, M., Kim, S., Machesky, J.E., Gentner, D.R., Robinson, A.L., Donahue, N.M., Presto, A.A., 2022. Limited secondary organic aerosol production from acyclic oxygenated volatile chemical products. Environ. Sci. Technol. 56, 4806–4815.
- Jiang, H., Ahmed, C.S., Zhao, Z., Chen, J.Y., Zhang, H., Canchola, A., Lin, Y.-H., 2020. Role of functional groups in reaction kinetics of dithiothreitol with secondary organic aerosols. Environ. Pollut. 263, 114402.

- Jiang, H., Jang, M., 2018. Dynamic oxidative potential of atmospheric organic aerosol under ambient sunlight. Environ. Sci. Technol. 52, 7496–7504.
- Jiang, H., Jang, M., Yu, Z., 2017. Dithiothreitol activity by particulate oxidizers of SOA produced from photooxidation of hydrocarbons under varied NO_X levels. Atmos. Chem. Phys. 17, 9965–9977.
- Jiang, H., Jang, M., Sabo-Attwood, T., Robinson, S.E., 2016. Oxidative potential of secondary organic aerosols produced from photooxidation of different hydrocarbons using outdoor chamber under ambient sunlight. Atmos. Environ. 131, 382–389.
- Kautzman, K.E., Surratt, J.D., Chan, M.N., Chan, A.W.H., Hersey, S.P., Chhabra, P.S., Dalleska, N.F., Wennberg, P.O., Flagan, R.C., Seinfeld, J.H., 2010. Chemical composition of gas-and aerosol-phase products from the photooxidation of naphthalene. J. Phys. Chem. A 114, 913–934.
- Kroll, J.H., Seinfeld, J.H., 2008. Chemistry of secondary organic aerosol: formation and evolution of low-volatility organics in the atmosphere. Atmos. Environ. 42, 3593–3624
- Kroll, J.H., Smith, J.D., Che, D.L., Kessler, S.H., Worsnop, D.R., Wilson, K.R., 2009. Measurement of fragmentation and functionalization pathways in the heterogeneous oxidation of oxidized organic aerosol. Phys. Chem. Chem. Phys. 11, 8005–8014.
- Lambe, A.T., Onasch, T.B., Croasdale, D.R., Wright, J.P., Martin, A.T., Franklin, J.P., Massoli, P., Kroll, J.H., Canagaratna, M.R., Brune, W.H., 2012. Transitions from functionalization to fragmentation reactions of laboratory secondary organic aerosol (SOA) generated from the OH oxidation of alkane precursors. Environ. Sci. Technol. 46, 5430–5437.
- Lambe, A.T., Onasch, T.B., Massoli, P., Croasdale, D.R., Wright, J.P., Ahern, A.T., Williams, L.R., Worsnop, D.R., Brune, W.H., Davidovits, P., 2011. Laboratory studies of the chemical composition and cloud condensation nuclei (CCN) activity of secondary organic aerosol (SOA) and oxidized primary organic aerosol (OPOA). Atmos. Chem. Phys. 11, 8913–8928.
- Laskin, A., Laskin, J., Nizkorodov, S.A., 2015. Chemistry of atmospheric brown carbon. Chem. Rev. 115, 4335–4382.
- Lauraguais, A., El Zein, A., Coeur, C., Obeid, E., Cassez, A., Rayez, M.-T., Rayez, J.-C., 2016. Kinetic study of the gas-phase reactions of nitrate radicals with methoxyphenol compounds: experimental and theoretical approaches. J. Phys. Chem. A 120, 2691–2699.
- Li, C., He, Q., Fang, Z., Brown, S.S., Laskin, A., Cohen, S.R., Rudich, Y., 2020. Laboratory insights into the diel cycle of optical and chemical transformations of biomass burning Brown carbon aerosols. Environ. Sci. Technol. 54, 11827–11837.
- Li, C., He, Q., Hettiyadura, A.P.S., Käfer, U., Shmul, G., Meidan, D., Zimmermann, R., Brown, S.S., George, C., Laskin, A., 2019a. Formation of secondary brown carbon in biomass burning aerosol proxies through NO₃ radical reactions. Environ. Sci. Technol. 54, 1395–1405.
- Li, C., He, Q., Schade, J., Passig, J., Zimmermann, R., Meidan, D., Laskin, A., Rudich, Y., 2019b. Dynamic changes in optical and chemical properties of tar ball aerosols by atmospheric photochemical aging. Atmos. Chem. Phys. 19, 139–163. https://doi. org/10.5194/acp-19-139-2019.
- Li, C., Hu, Y., Zhang, F., Chen, J., Ma, Z., Ye, X., Yang, X., Wang, L., Tang, X., Zhang, R., 2017. Multi-pollutant emissions from the burning of major agricultural residues in China and the related health-economic effects. Atmos. Chem. Phys. 17, 4957–4988.
- Li, X., Tao, Y., Zhu, L., Ma, S., Luo, S., Zhao, Z., Sun, N., Ye, Z., Ge, X., 2022. Optical properties and oxidative potential of aqueous-phase products from OH and ³C*initiated photolysis of eugenol. Atmos. Chem. Phys. 22, 7793–7814.
- Li, Y., Pöschl, U., Shiraiwa, M., 2016. Molecular corridors and parameterizations of volatility in the chemical evolution of organic aerosols. Atmos. Chem. Phys. 16, 3327–3344. https://doi.org/10.5194/acp-16-3327-2016.
- 3327–3344. https://doi.org/10.5194/acp-16-3327-2016.
 Li, Y.J., Huang, D.D., Cheung, H.Y., Lee, A.K.Y., Chan, C.K., 2014. Aqueous-phase photochemical oxidation and direct photolysis of vanillin-a model compound of methoxy phenols from biomass burning. Atmos. Chem. Phys. 14, 2871–2885.
- Lin, M., Yu, J.Z., 2019. Dithiothreitol (DTT) concentration effect and its implications on the applicability of DTT assay to evaluate the oxidative potential of atmospheric aerosol samples. Environ. Pollut. 251, 938–944. https://doi.org/10.1016/j. envpol.2019.05.074.
- Lin, P., Fleming, L.T., Nizkorodov, S.A., Laskin, J., Laskin, A., 2018. Comprehensive molecular characterization of atmospheric brown carbon by high resolution mass spectrometry with electrospray and atmospheric pressure photoionization. Anal. Chem. 90, 12493–12502.
- Lin, P., Liu, J., Shilling, J.E., Kathmann, S.M., Laskin, J., Laskin, A., 2015. Molecular characterization of brown carbon (BrC) chromophores in secondary organic aerosol generated from photo-oxidation of toluene. Phys. Chem. Chem. Phys. 17, 23312–23325.
- Liu, C., Liu, J., Liu, Y., Chen, T., He, H., 2019. Secondary organic aerosol formation from the OH-initiated oxidation of guaiacol under different experimental conditions. Atmos. Environ. 207, 30–37.
- Liu, P.F., Abdelmalki, N., Hung, H.-M., Wang, Y., Brune, W.H., Martin, S.T., 2015. Ultraviolet and visible complex refractive indices of secondary organic material produced by photooxidation of the aromatic compounds toluene and m-xylene. Atmos. Chem. Phys. 15, 1435–1446.
- Ma, X., Nie, D., Chen, M., Ge, P., Liu, Z., ge, X., Li, Z., Gu, R., 2021. The relative contributions of different chemical components to the oxidative potential of ambient fine particles in nanjing area. Int. J. Environ. Res. Publ. Health 18, 2789. https://doi. org/10.3390/ijerph18062789.
- Mao, J., Ren, X., Brune, W.H., Olson, J.R., Crawford, J.H., Fried, A., Huey, L.G., Cohen, R.C., Heikes, B., Singh, H.B., 2009. Airborne measurement of OH reactivity during INTEX-B. Atmos. Chem. Phys. 9, 163–173.
- Mayorga, R.J., Zhao, Z., Zhang, H., 2021. Formation of secondary organic aerosol from nitrate radical oxidation of phenolic VOCs: implications for nitration mechanisms

- and brown carbon formation. Atmos. Environ. 244, 117910 https://doi.org/10.1016/j.atmosenv.2020.117910.
- Mertes, P., Pfaffenberger, L., Dommen, J., Kalberer, M., Baltensperger, U., 2012. Development of a sensitive long path absorption photometer to quantify peroxides in aerosol particles (Peroxide-LOPAP). Atmos. Meas. Tech. 5, 2339–2348.
- Misovich, M.V., Hettiyadura, A.P.S., Jiang, W., Zhang, Q., Laskin, A., 2021. Molecular-level study of the photo-oxidation of aqueous-phase guaiacyl acetone in the presence of 3C*: formation of Brown carbon products. ACS Earth Space Chem 5, 1983–1996.
- Pardo, M., Li, C., Fang, Z., Levin-Zaidman, S., Dezorella, N., Czech, H., Martens, P., Käfer, U., Gröger, T., Rüger, C.P., 2021. Toxicity of water-and organic-soluble wood tar fractions from biomass burning in lung epithelial cells. Chem. Res. Toxicol. 34, 1588–1603. https://doi.org/10.1021/acs.chemrestox.1c00020.
- Pardo, M., Li, C., He, Q., Levin-Zaidman, S., Tsoory, M., Yu, Q., Wang, X., Rudich, Y., 2020. Mechanisms of lung toxicity induced by biomass burning aerosols. Part. Fibre Toxicol 17, 1–15. https://doi.org/10.1186/s12989-020-0337-x.
- Qi, X., Zhu, S., Zhu, C., Hu, J., Lou, S., Xu, L., Dong, J., Cheng, P., 2020. Smog chamber study of the effects of NO_x and NH₃ on the formation of secondary organic aerosols and optical properties from photo-oxidation of toluene. Sci. Total Environ. 727, 138632 https://doi.org/10.1016/j.scitotenv.2020.138632.
- Roach, P.J., Laskin, J., Laskin, A., 2011. Higher-order mass defect analysis for mass spectra of complex organic mixtures. Anal. Chem. 83, 4924–4929.
- Roldin, P., Ehn, M., Kurtén, T., Olenius, T., Rissanen, M.P., Sarnela, N., Elm, J., Rantala, P., Hao, L., Hyttinen, N., 2019. The role of highly oxygenated organic molecules in the Boreal aerosol-cloud-climate system. Nat. Commun. 10, 1–15.
- Sarrafzadeh, M., Wildt, J., Pullinen, I., Springer, M., Kleist, E., Tillmann, R., Schmitt, S. H., Wu, C., Mentel, T.F., Zhao, D., 2016. Impact of NO_X and OH on secondary organic aerosol formation from β -pinene photooxidation. Atmos. Chem. Phys. 16, 11237–11248.
- Sato, K., Takami, A., Kato, Y., Seta, T., Fujitani, Y., Hikida, T., Shimono, A., Imamura, T., 2012. AMS and LC/MS analyses of SOA from the photooxidation of benzene and 1, 3, 5-trimethylbenzene in the presence of NO_x: effects of chemical structure on SOA aging. Atmos. Chem. Phys. 12, 4667–4682.
- Schuchardt, S., Kruse, H., 2009. Quantitative volatile metabolite profiling of common indoor fungi: relevancy for indoor air analysis. J. Basic Microbiol. 49, 350–362.
- Seitz, L.M., Ram, M.S., 2000. Volatile methoxybenzene compounds in grains with offodors. J. Agric. Food Chem. 48, 4279–4289.
- Sekimoto, K., Koss, A.R., 2021. Modern mass spectrometry in atmospheric sciences: measurement of volatile organic compounds in the troposphere using protontransfer-reaction mass spectrometry. J. Mass Spectrom. 56, e4619.
- SriBala, G., Carstensen, H.-H., Van Geem, K.M., Marin, G.B., 2019. Measuring biomass fast pyrolysis kinetics: state of the art. Wiley Interdiscip. Rev. Energy Environ. 8, e326
- Sun, J., Cao, H., Zhang, S., Li, X., He, M., 2016. Theoretical study on the mechanism of the gas phase reaction of methoxybenzene with ozone. RSC Adv. 6, 113561–113569. https://doi.org/10.1039/C6RA22286B.
- Toloza, A.C., Zygadlo, J., Cueto, G. mougabure, Biurrun, F., Zerba, E., Picollo, M.I., 2006. Fumigant and repellent properties of essential oils and component compounds against permethrin-resistant Pediculus humanus capitis (Anoplura: pediculidae) from Argentina. J. Med. Entomol. 43, 889–895. https://doi.org/10.1093/jmedent/435.889
- Tong, H., Zhang, Y., Filippi, A., Wang, T., Li, C., Liu, F., Leppla, D., Kourtchev, I., Wang, K., Keskinen, H.-M., Levula, J.T., Arangio, A.M., Shen, F., Ditas, F., Martin, S. T., Artaxo, P., Godoi, R.H.M., Yamamoto, C.I., de Souza, R.A.F., Huang, R.-J., Berkemeier, T., Wang, Y., Su, H., Cheng, Y., Pope, F.D., Fu, P., Yao, M., Pöhlker, C., Petäjä, T., Kulmala, M., Andreae, M.O., Shiraiwa, M., Pöschl, U., Hoffmann, T., Kalberer, M., 2019. Radical formation by fine particulate matter associated with highly oxygenated molecules. Environ. Sci. Technol. 53, 12506–12518. https://doi.org/10.1021/acs.est.9005149
- Tuet, W.Y., Chen, Y., Xu, L., Fok, S., Gao, D., Weber, R.J., Ng, N.L., 2017. Chemical oxidative potential of secondary organic aerosol (SOA) generated from the photooxidation of biogenic and anthropogenic volatile organic compounds. Atmos. Chem. Phys. 17, 839–853. https://doi.org/10.5194/acp-17-839-2017.
- Wagnon, S.W., Thion, S., Nilsson, E.J.K., Mehl, M., Serinyel, Z., Zhang, K., Dagaut, P., Konnov, A.A., Dayma, G., Pitz, W.J., 2018. Experimental and modeling studies of a biofuel surrogate compound: laminar burning velocities and jet-stirred reactor measurements of anisole. Combust. Flame 189, 325–336. https://doi.org/10.1016/j. combustflame.2017.10.020.
- Wagnon, S.W., Thion, S., Nilsson, E.K., Mehl, M., Serinyel, Z., Zhang, K., Dagaut, P., Konnov, A.A., Dayma, G., Pitz, W.J., 2017. The Development and Validation of a Chemical Kinetic Model for Anisole, a Compound to Represent Biomass Pyrolysis Fuels. Lawrence Livermore National Lab.(LLNL), Livermore, CA (United States).
- Wang, S., Takhar, M., Zhao, Y., Chan, A.W.H., 2021. Dynamic oxidative potential of organic aerosol from heated cooking oil. ACS Earth Space Chem 1150–1162. https:// doi.org/10.1021/acsearthspacechem.1c00038.
- Wang, S., Ye, J., Soong, R., Wu, B., Yu, L., Simpson, A.J., Chan, A.W., 2018. Relationship between chemical composition and oxidative potential of secondary organic aerosol from polycyclic aromatic hydrocarbons. Atmos. Chem. Phys. 18, 3987–4003.
- Wojcieszyk, M., Knuutila, L., Kroyan, Y., de Pinto Balsemão, M., Tripathi, R., Keskivali, J., Karvo, A., Santasalo-Aarnio, A., Blomstedt, O., Larmi, M., 2021. Performance of anisole and isobutanol as gasoline bio-blendstocks for spark ignition engines. Sustainability 13, 8729.
- Wu, Y., Rossow, B., Modica, V., Yu, X., Wu, L., Grisch, F., 2017. Laminar flame speed of lignocellulosic biomass-derived oxygenates and blends of gasoline/oxygenates. Fuel 202, 572–582.

- Yang, X., Liu, Y.-B., 2021. Anisole is an environmentally friendly fumigant for postharvest pest control. J. Stored Prod. Res. 93, 101842 https://doi.org/10.1016/j. jspr.2021.101842.
- Yu, L., Smith, J., Laskin, A., Anastasio, C., Laskin, J., Zhang, Q., 2014. Chemical characterization of SOA formed from aqueous-phase reactions of phenols with the triplet excited state of carbonyl and hydroxyl radical. Atmos. Chem. Phys. 14, 13801–13816
- Zawadowicz, M.A., Lee, B.H., Shrivastava, M., Zelenyuk, A., Zaveri, R.A., Flynn, C., Thornton, J.A., Shilling, J.E., 2020. Photolysis controls atmospheric budgets of biogenic secondary organic aerosol. Environ. Sci. Technol. 54, 3861–3870.
- Zhao, D., Schmitt, S.H., Wang, M., Acir, I.-H., Tillmann, R., Tan, Z., Novelli, A., Fuchs, H., Pullinen, I., Wegener, R., 2018. Effects of NO_x and SO₂ on the secondary organic

aerosol formation from photooxidation of $\alpha\text{-pinene}$ and limonene. Atmos. Chem. Phys. 18, 1611–1628.

Chemosphere 308 (2022) 136421

- Zhao, R., Zhang, Q., Xu, X., Zhao, W., Yu, H., Wang, W., Zhang, Y., Zhang, W., 2021.
 Effect of experimental conditions on secondary organic aerosol formation in an oxidation flow reactor. Atmos. Pollut. Res. 12, 205–213.
- Zhang, Z.-H., Hartner, E., Utinger, B., Gfeller, B., Paul, A., Sklorz, M., Czech, H., Yang, B. X., Su, X.Y., Jakobi, G., 2022. Are reactive oxygen species (ROS) a suitable metric to predict toxicity of carbonaceous aerosol particles? Atmos. Chem. Phys. 22, 1793–1809.
- Zhu, J., Shang, J., Chen, Y., Kuang, Y., Zhu, T., 2020. Reactive oxygen species-related inside-to-outside oxidation of soot particles triggered by visible-light irradiation: physicochemical property changes and oxidative potential enhancement. Environ. Sci. Technol. 54, 8558–8567. https://doi.org/10.1021/acs.est.0c01150.
- Ziemann, P.J., Atkinson, R., 2012. Kinetics, products, and mechanisms of secondary organic aerosol formation. Chem. Soc. Rev. 41, 6582.